Ti_3O_5 monolayer: Tunable quantum anomalous Hall insulator

Xiaokang Xu,[1] Tianxia Guo,[1] Donghao Guan,[1] Jie Li,[1] Ailei He,[1,*] Jinlian Lu,[2] Xiaojing Yao,[3] Yongjun Liu,[1,†] and Xiuyun Zhang[1,4,‡]

[1]*College of Physics Science and Technology, Yangzhou University, Yangzhou 225002, China*

[2]*Department of Physics, Yancheng Institute of Technology, Yancheng, Jiangsu 224051, China*

[3]*College of Physics and Hebei Advanced Thin Films Laboratory, Hebei Normal University, Shijiazhuang 050024, China*

[4]*Key Laboratory of Quantum Materials and Devices (Southeast University), Ministry of Education, Nanjing 20089, China*

(Received 5 October 2023; revised 17 November 2023; accepted 5 December 2023; published 21 December 2023)

The quantum anomalous Hall (QAH) effect has attracted significant attention due to its potential applications in low-power-consumption spintronic devices. In this study, we performed density functional theory calculations to investigate the stability, electronic, and topological properties of Ti_3O_5 monolayer. Our results demonstrate that Ti_3O_5 monolayer is thermally and dynamically stable. In the absence of spin-orbit coupling (SOC), the monolayer exhibits spin-polarized Weyl semimetal behavior and the Weyl points are protected by the vertical mirror symmetry. Specifically, the Weyl points can be preserved when the magnetization direction is parallel to *xoy* plane. By altering the magnetization direction out of plane, the Weyl points are opened and the system is transformed into the QAH phase ($|C| = 1$). To validate our findings, we constructed a 12-band tight-binding model based on first-principles calculations, which successfully reproduces the QAH state by incorporating exchange coupling and the SOC term. Furthermore, it is observed that a transition from ferromagnetic QAH insulator to antiferromagnetic semiconductor occurs when biaxial compressive strain is applied. These results open up exciting possibilities for the realization of two-dimensional Weyl semimetals and the QAH effect in a single material, which has significant applications for the fields of spintronics and topological microelectronics.

DOI: 10.1103/PhysRevB.108.214427

I. INTRODUCTION

Since the discovery of quantized Hall conductance in two-dimensional (2D) electron gas under low temperature and strong magnetic field by Klitzing [1], various quantum Hall effects have attracted enormous interest in condensed matter physics and materials science. Among them, the quantum anomalous Hall (QAH) effect is an exotic topological quantum state in 2D magnetic materials, which exhibits quantized Hall conductance even at zero external magnetic field [1,2]. The QAH effect can be characterized by the nonzero Chern number (C) and chiral conductive edge states within the insulating bulk. The chiral edge states are dissipationless without affecting by the perturbations and disorders, which provides great potential applications for next-generation low-power-consumption spintronic devices. Besides, QAH insulators provide an excellent platform to investigate interesting topological phases such as topological superconductors [3], axion insulators [4,5], and so on.

The QAH effect was proposed by Haldane via applying staggered magnetic flux in a honeycomb lattice [2]. Afterwards, a number of QAH materials were synthesized experimentally and predicted theoretically. As the realization of the QAH needs to break the time reversal symmetry T, it is necessary to introduce magnetic elements like d/f transition metals (TMs) in 2D candidates. An early observation of QAH effect was the Cr-doped (Bi, $Sb)_2Te_3$ in ultralow temperature (~30 mK) [6]. Similarly, the *V-I* codoped Sb_2Te_3 [7] or TM atom doped graphene [8–10] were also identified to be QAH insulators. Unfortunately, the long-range ferromagnetic (FM) order is unstable and the magnetic homogeneity is difficult to control by magnetic doping approaches. Besides, the QAH effect can be achieved by stacking homo- or heterolayers, such as ferromagnetic/quantum spin Hall (FM/QSH) heterostructures [8,11–15], layered $MnBi_2Te_4$ family [16,17], twisted bilayer graphene [18–21], and so on. Moreover, the intrinsic QAH materials have also been predicted theoretically in 2D magnetic insulators, including metal-organic frameworks [22–26], TM trihalides [27–29], TM oxides [30–33], etc.

Despite the progress, the discovery of 2D intrinsic QAH insulators remains a challenge due to the difficulty of maintaining long-range magnetic orders in the presence of strong thermal fluctuations, as indicated by the Mermin-Wagner theorem [34]. Moreover, to change the direction of the edge channel in most QAH systems, the large magnetic field is required to reverse the magnetization direction. In this study, we performed a comprehensive investigation of the stability, electronic, and topological properties of a 2D triangular Ti_3O_5 monolayer using density functional theory (DFT) calculations. Our findings suggest that the structure of the Ti_3O_5 monolayer is thermally and dynamically stable. In the absence of spin-orbit coupling (SOC), Ti_3O_5 monolayer exhibits spin-polarized Weyl semimetal behavior. Specifically,

*heailei@yzu.edu.cn

†yjliu@yzu.edu.cn

‡xyzhang@yzu.edu.cn

the Weyl points can survive against SOC when the magnetization direction is along the *xoy* plane. In contrast, when the magnetization direction is along the *z* axis, the Weyl points are opened up and the monolayer is transformed into the QAH phase with Chern number $|C| = 1$. Moreover, a 12-band tight-binding (TB) model was constructed based on first-principles calculations to validate the results, which successfully reproduces the QAH state by incorporating exchange coupling and SOC. Additionally, we observed a phase transition from a FM QAH insulator to an antiferromagnetic (AFM) semiconductor (SC) under biaxial compressive strain.

II. COMPUTATIONAL METHODS

All the calculations were carried out with projector-augmented wave (PAW) [35] methods within Vienna *ab initio* Simulation Package (VASP) [36,37]. The exchange-correlation potential was adopted by the generalized gradient approximation (GGA) of the Perdew-Burke-Ernzerhof (PBE) functional [38–42]. The cutoff energy was set as 500 eV. The energy and force convergence criteria were set to be 10^{-7} eV and 0.001 eV/Å, respectively. The vacuum slab of 20 Å was applied to avoid the physical interactions of periodic cells. For geometry optimization, the first Brillouin zone was sampled by Γ-centered k mesh of $12 \times 12 \times 1$. The correlation effects for the Ti − 3d electrons were treated by the DFT + U ($U_{\mathrm{eff}} = 4$ eV) method [43–45]. Phonon dispersions were calculated using $4 \times 4 \times 1$ supercells by PHONOPY code on the basis of density functional perturbation theory (DFPT) [46]. The Monte Carlo (MC) simulations based on the classical Heisenberg model were performed to estimate the Curie temperature (T_C) [47]. The TB Hamiltonian was constructed in the WANNIER90 package [48] with the maximally localized Wannier functions (MLWF) [49]. The edge states were calculated by the WANNIERTOOLS package [50].

III. RESULTS

As illustrated in Fig. 1(a), the Ti_3O_5 monolayer is a triangular lattice consisting of one hexagonal Ti-O layer sandwiched by two hexagonal O layers. Each Ti atom in the structure is bonded with five O atoms around. One O atom (called O_1) per unit cell lies in the middle Ti triangular lattice, and the other four O atoms (called O_2) sit directly above and below the hollow sites of the middle Ti−O_1 triangular lattice, as marked in the side view in Fig. 1(a). The lattice constant of Ti_3O_5 monolayer is 5.12 Å and the space group of it is $P\bar{6}2m$, which is generated by a threefold rotation symmetry C_{3z}, a vertical mirror symmetry M_y, and a horizontal mirror symmetry M_z. The distance between adjacent O_2 atoms (O_2−O_2 bond) is about 2.37 Å. The Ti-O_2 and Ti-Ti bond lengths are 1.93 and 2.74 Å, and the Ti-O_2-Ti angle (α) and O_2-Ti-O_2 angle (β) are 88.38° and 95.62°, respectively. The thermal stability of Ti_3O_5 monolayer was evaluated by MD simulations. The snapshot at the end of 6 ps at 300 K is shown in Fig. 1(b); it is suggested that the thermal-induced fluctuations induce slight changes in geometry, indicating that the Ti_3O_5 monolayer maintains its structural integrity and has good thermal stability at room temperature. The lattice dynamical stability

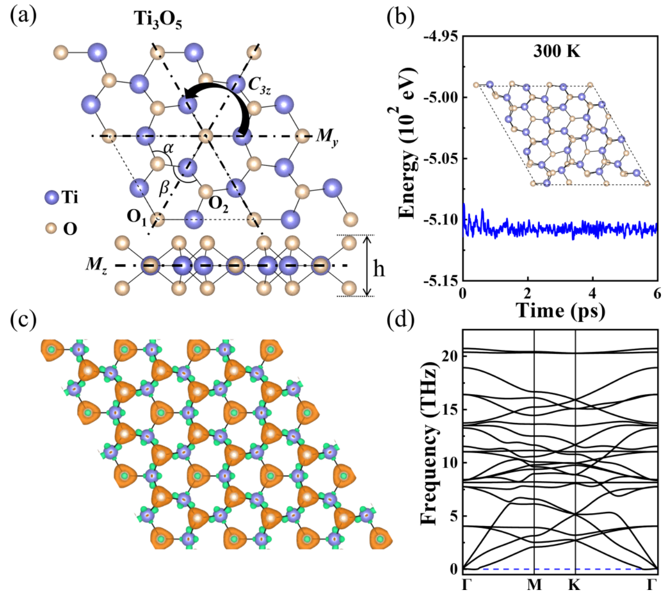

FIG. 1. (a) Top and side views of Ti_3O_5 monolayer. (b) The snapshot of Ti_3O_5 monolayer at the end of 6 ps at 300 K. (c) Charge density difference and (d) the phonon dispersion spectra of Ti_3O_5 monolayer; the orange and green colors represent electron accumulation and depletion, respectively.

of the Ti_3O_5 monolayer is confirmed by analyzing the phonon dispersion spectra. As shown in Fig. 1(d), there are no imaginary frequencies in the whole Brillouin zone, indicating that Ti_3O_5 monolayer is dynamically stable. The formation energy of Ti_3O_5 monolayer is calculated as

$$E_f = [E_{\mathrm{Ti3O5}} - 3 \times E_{\mathrm{Ti}} - 5 \times E_{\mathrm{O}}]/8, \quad (1)$$

where E_{Ti}, E_{O}, and E_{Ti3O5} are the chemical potential of the Ti atom and the O atom, and the energy of Ti_3O_5 monolayer, respectively. The calculated E_f is −0.99 eV, indicating the formation of Ti_3O_5 monolayer is energetically favorable. Mimicking other van der Waals layered materials, we calculated the exfoliation energy of Ti_3O_5 monolayer, and the calculated value is 0.54 Jm^2, which is below the easily exfoliation limit [51]. As shown in the charge density difference in Fig. 1(c), electron accumulation and depletion occur on Ti and O atoms, respectively. Bader charge analysis suggests that about two (one) electrons are transferred from Ti atoms to O_1 (O_2) atoms.

To explore the magnetic ground state of Ti_3O_5 monolayer, one FM and two AFM (AFM1, AFM2) configurations are considered, as displayed in Fig. S1 in the Supplemental Material [52]. Our results show that the system favors the FM ground state, which is about 34.3 and 101.8 meV per unit cell lower in energy than AFM1 and AFM2 states, respectively. The spin density plots of FM Ti_3O_5 monolayer are shown in Fig. 2(c), and the total magnetic moment per unit cell is 2.0 μ_B. The FM order of Ti atoms is determined by the superexchange mechanism. As mentioned above, the Ti-Ti bond is much longer than the Ti-O bond, indicating that the direct exchange is weak. Moreover, the Ti-O-Ti bond angle is 88.38°, approaching 90°, which leads to the strong FM coupling according to Goodenough-Kanamori-Anderson (GKA)

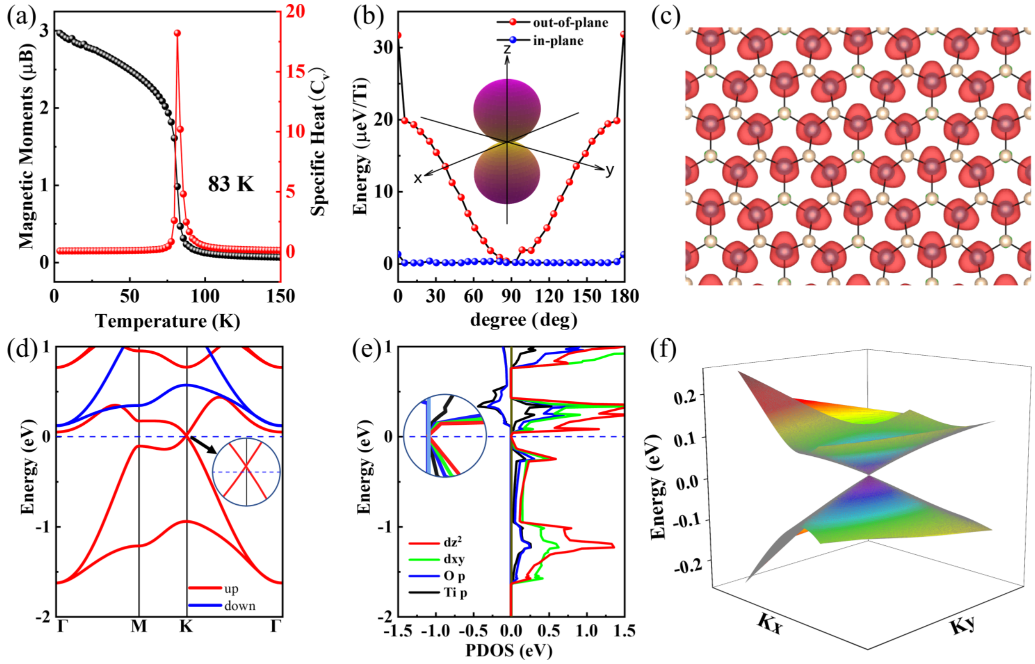

FIG. 2. (a) Monte Carlo simulation results for the specific heat and magnetic moments as a function of temperature. (b) The angular dependence of MAE of Ti_3O_5 monolayer. (c) Spin density plot, (d) the electronic band structure, and (e) projected density of states of Ti_3O_5 monolayer. (f) 3D band structure of Ti_3O_5 monolayer.

rules [53–55]. To measure of the stability of the FM system, the Curie temperature (T_C) is explored. Here, Monte Carlo (MC) simulations are conducted using the 2D Heisenberg Hamiltonian model to investigate the spin dynamics of FM Ti_3O_5 monolayer; the Hamiltonian is written as

$$H = -\sum_{\langle ij\rangle} J_1 \vec{S}_i \vec{S}_j - \sum_{\langle\langle ij\rangle\rangle} J_2 \vec{S}_i \vec{S}_j \tag{2}$$

where J_1 and J_2 are the nearest neighboring (NN) and next-nearest neighboring (NNN) exchange coupling parameters, respectively, and $\vec{S}_i$ is the spin vector at the site i. The calculated J_1 and J_2 are −50.7 and 36.9 meV, respectively. Based on Monte Carlo simulation, T_C can be extracted from the peak of specific heat when the system reaches equilibrium at a given temperature. As exhibited in Fig. 2(a), the T_C of Ti_3O_5 monolayer is 83 K. The magnetic anisotropic energies (MAEs) of Ti_3O_5 monolayer with magnetization in plane and out of plane are shown in Fig. 2(b), which illustrates that magnetic easy axis lies in the xoy plane with the MAE value of about 31.7 μeV per Ti atom.

The spin-polarized band structure and projected density of states (PDOS) of Ti_3O_5 monolayer are shown in Figs. 2(d)–2(f). The monolayer is found to be half semimetal, in which the spin up channel is half metallic with a Weyl point crossing at the high symmetry K point of Fermi level; in contrast, the spin down channel shows a semiconducting feather with the band gap of 2.76 eV. The PDOS plot shows that the magnetism of the systems is mainly contributed by $3d$ orbitals of the Ti atom, and the Weyl point near the Fermi level is mainly contributed by Ti-dz^2/Ti-d_{xy}, and O-p orbitals. By considering SOC, various topological phases sensitive to the magnetization orientation are found. As shown in Fig. 3(a), when the magnetization direction is along y axis, the C_{3z} symmetry and M_z symmetry are broken, while M_y symmetry remains. Furthermore, when we artificially break the M_y symmetry by moving one pair of O_2 atoms along the $+y$ axis (see Fig. S2 in the Supplemental Material [52]), the Weyl point is opened. Therefore, we can conclude that it is the existence of M_y symmetry that protects the Weyl point. When applying in-plane

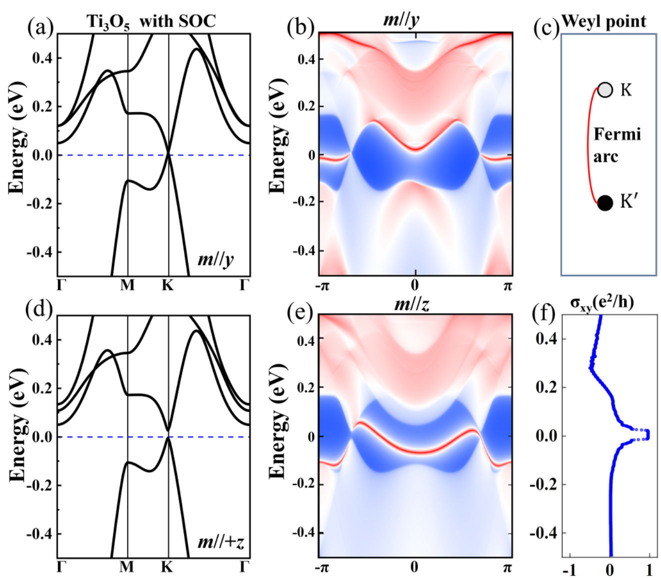

FIG. 3. (a) The band structure and (b) edge state of Ti_3O_5 monolayer in the presence of SOC and magnetization lying along y axis. (c) The schematics of Weyl points and Fermi arc. (d) The band structure, (e) edge state, and (f) anomalous Hall conductivity in the presence of SOC when magnetization lies along $+z$ axis.

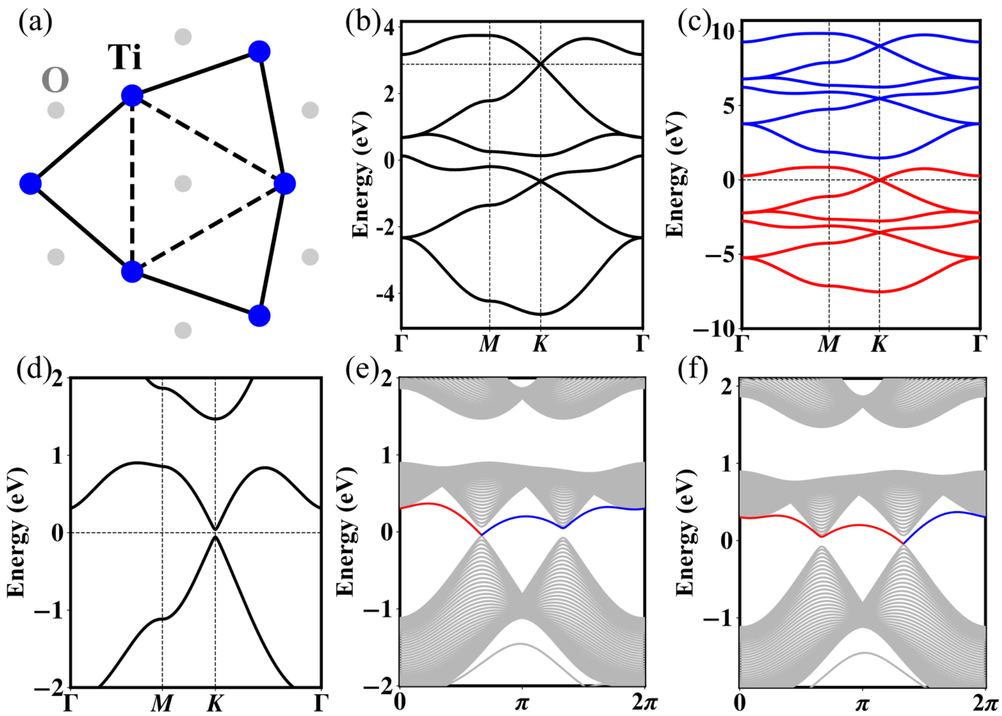

FIG. 4. (a) Three sites triangle lattice with solid and dashed lines representing NN and NNN hopping potential, respectively. Each site contains d_{xy} and dz^2 electrons of Ti. Ti, O atoms are displayed by blue, grey. Band structure with (b) $\lambda = 0$ eV, $E_{\text{ex}} = 0$ eV, (c) $\lambda = 0$ eV, $E_{\text{ex}} = 4.5$ eV, (d) $\lambda = 0.05$ eV, $E_{\text{ex}} = 4.5$ eV. The cylinder geometry with (e) $\lambda = 0.05$ eV, $E_{\text{ex}} = 4.5$ eV, (f) $\lambda = -0.05$ eV, $E_{\text{ex}} = 4.5$ eV; in both cases $t_{1dxy} = 1$ eV, $t_{2dxy} = -1.05$ eV, $t^2_{1dz} = 0.3$ eV, $t^2_{2dz} = 0.1$ eV, $t^3 = 1.5$ eV.

magnetization, the variation of magnetization direction does not open the Weyl point at the Fermi level (see Fig. S3 [52]).

The edge state of the semi-infinite nanoribbon is presented in Fig. 3(b), in which two Weyl points are connected by a Fermi arc. In Fig. 3(c), the Berry phases around the K (K') points of the Ti_3O_5 monolayer are schematically depicted by white and black cycles, respectively. The corresponding Berry phase are given as 0.998π and -0.997π, indicating that the Berry curvatures around K (K') points behave as monopoles with positive (negative) chirality. To achieve a QAH state, it is crucial to break all vertical mirrors symmetries [31,56–58]. By applying the magnetization along the $+z$ axis, the M_y symmetry in the Ti_3O_5 monolayer is broken and the Weyl points disappear. As displayed in Fig. 3(d), the Ti_3O_5 monolayer is turned to be QAH insulator with a band gap of 30 meV. The edge state of a semi-infinite nanoribbon is displayed in Fig. 3(e); the chiral edge state connects the valence and conduction bands in the bulk gap. To identify the topological invariant of the QAH state, we calculate the Chern number by

$$C = \frac{1}{2\pi}\int_{BZ} dk^2 \Omega_n(\mathbf{k}), \tag{3}$$

where Ω represents the Berry curvature in the momentum space. There are two Weyl points in the whole Brillouin zone (BZ); each opened Weyl point donates a topological charge of 0.5. Therefore, the Ti_3O_5 monolayer displays a QAH state with Chern number $C = 1$ and the anomalous Hall conductance exhibits a quantized plateau ($\sigma_{xy} = e^2/h$) [see Fig. 3(f)]. Due to the extremely low MAE of the Ti_3O_5 monolayer, the magnetization direction can be readily influenced and altered by the application of a small external magnetic field. As illustrated in Fig. S4 in the Supplemental Material [52], when the magnetization direction is along the $-z$ axis, the chiral edge state changes its direction with Chern number $C = -1$.

To deeply investigate the electronic properties of Ti_3O_5 monolayer in parameter space, we constructed a tight-binding (TB) model based on density functional theory (DFT) results. Based on the above discussion, the dz^2 and d_{xy} orbitals are dominant electronic states around the Fermi level; the Hamiltonian is built based on dz^2 and d_{xy} orbitals of three Ti atoms with SOC and an effective exchange field [see Fig. 4(a)]. The Hamiltonian can be written as

$$H = H_0 + H_{\text{SOC}} + H_{EX}, \tag{4}$$

$$H_0 = \sum_{i,j} C_i^+ H_{NN} C_j + \sum_{i,j} C_i^+ H_{NNN} C_j + t_3 \sum_i C_i^+ \sigma_x \sigma_0 C_i, \tag{5}$$

$$H_{\text{SOC}} + H_{EX} = \sum_{i,j} C_i^+ H_{ij} C_j - E_{ex} \sum_i C_i^+ \sigma_z \sigma_0 C_i, \tag{6}$$

where $C_i^+ = (C^+_{idxy\uparrow}, C^+_{idxy\downarrow}, C^+_{idz^2\uparrow}, C^+_{idz^2\downarrow})$ is the creation operator of the electrons on the orbitals $d_{xy}\uparrow$, $d_{xy}\downarrow$, $dz^2\uparrow$, $dz^2\downarrow$ on site i, $\sigma_0, \sigma_x, \sigma_z$ is the 2×2 unit matrix and spin Pauli matrix along the x and z direction, respectively. $H_{NN} = \left[\begin{smallmatrix} t_{1dxy} & 0 \\ 0 & t_{1dz^2} \end{smallmatrix}\right]\sigma_0$ and $H_{NNN} = \left[\begin{smallmatrix} t_{2dxy} & 0 \\ 0 & t_{2dz^2} \end{smallmatrix}\right]\sigma_0$ are the NN and NNN hopping potentials, and t_3 represents the hopping potential between d_{xy} and dz^2 electrons on the ith site. The first term of Eq. (6) denotes SOC energy with $H_{ii} = \lambda\left[\begin{smallmatrix} 0 & i\sigma_z \\ -i\sigma_z & 0 \end{smallmatrix}\right]$, where λ is the SOC strength. In the second term of Eq. (6), E_{ex} is the strength of exchange splitting. As shown in Fig. 4(b), a

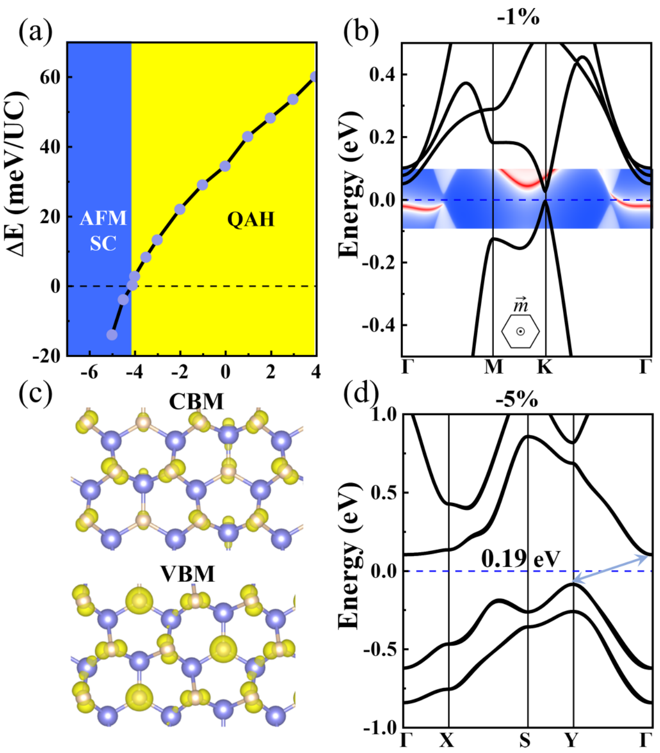

FIG. 5. (a) The function of the energy difference between FM and lowest energy AFM state of Ti_3O_5 monolayer with the biaxial strains ranging −5% to 4%. (b) The band structure and edge state of Ti_3O_5 monolayer at $\eta = -1\%$. (c) The charge density of CBM, VBM, and (d) band structure of AFM1 at $\eta = -5\%$.

Dirac point is presented without considering the SOC term and exchange field term. Once the exchange field is taken into account, the system turns to be a spin-polarization Weyl semimetal [see Fig. 4(c)]. Afterwards, when the SOC term ($\lambda = 0.05$ eV) is involved, the Weyl point is gapped with $C = 1$ [see Figs. 4(d) and 4(e)]. As displayed in Fig. 4(f), when we change the sign of the SOC term, the direction of the edge state reverses with $C = -1$, which is consistent with the DFT calculation.

Additionally, we investigate the effect of biaxial tensile strains on the topological properties of Ti_3O_5 monolayer. The strain intensity is defined as $\eta = (a - a_0)/a_0 \times 100\%$, and the negative (positive) values of η stand for the compressive (tensile) strains. The energy differences between the FM and AFM1 states from $\eta = -5\%$ to 4% are shown in Fig. 5(a). Notably, the ground state of the Ti_3O_5 monolayer is transited from the QAH insulator to the AFM1 SC under 4.1% compressive strain. Figure 5(b) displays the electronic band structure and edge state of the Ti_3O_5 monolayer at $\eta = -1\%$. It is QAH with $C = 1$, with one edge state connecting the conducting band and valence band. Figures 5(c) and 5(d) illustrate the charge density of the conduction band minimum (CBM), valance band maximum (VBM), and band structure of Ti_3O_5 monolayer under −5% strain. Clearly, it is a semiconductor with a band gap of 0.19 eV, in which the CBM and VBM are mainly composed of d_{xy}, dx^2, dz^2 orbitals of Ti atoms. Therefore, the property of Ti_3O_5 monolayer can be manipulated by external strains. Moreover, the easy magnetization axis of monolayer Ti_3O_5 varies with the external strains. When applying tensile strains, the easy magnetization axis of monolayer Ti_3O_5 remains in-plane and the MAE value gradually increases with η ranging 1–4%. By applying compressive strains, the easy magnetization axis of monolayer Ti_3O_5 turns to be out-of-plane and the MAE values decrease with $\eta = -1\%$ to −3%, then it turns to be in-plane at $\eta = -4\%$ (see Fig. S6 [52]).

IV. CONCLUSION

In conclusion, by using density functional theory (DFT) calculations, we systematically investigate the 2D FM Ti_3O_5 monolayer with $T_C = 83$ K. In the absence of SOC, the monolayer is a spin-polarized Weyl semimetal. When SOC is considered, the Weyl points survive with the protection of the vertical mirror symmetry M_y. Breaking the M_y mirror symmetry by applying vertical magnetic field leads to a phase transition from a Weyl semimetal to a QAH insulator with a Chern number $|C| = 1$. Moreover, we constructed a 12-band TB model based on first-principles calculations. This TB model successfully reproduced the QAH state by incorporating exchange coupling and SOC. Furthermore, a phase transition from a FM QAH insulator to an AFM SC is observed under biaxial compressive strain. Overall, our study provides valuable insights into the properties of the Ti_3O_5 monolayer and highlights its potential for applications in spintronics and quantum computing.

ACKNOWLEDGMENTS

This work was supported by the National Natural Science Foundation of China (Grants No. 12204404, No. 12004098, No. 12004328), the Six Talent Peaks Project in Jiangsu Province (Project No. XCL-104), the open research fund of Key Laboratory of Quantum Materials and Devices (Southeast University), Ministry of Education, and the funding for school-level research projects of Yancheng Institute of Technology (Grant No. xjr2019053).

X.K.X., T.X.G., and D.H.G. contributed equally to this work.

[1] K. v. Klitzing, G. Dorda, and M. Pepper, New method for high-accuracy determination of the fine-structure constant based on quantized Hall resistance, Phys. Rev. Lett. **45**, 494 (1980).

[2] F. D. M. Haldane, Model for a quantum Hall effect without Landau levels: Condensed-matter realization of the “parity anomaly”, Phys. Rev. Lett. **61**, 2015 (1988).

[3] X. L. Qi, T. L. Hughes, and S. C. Zhang, Chiral topological superconductor from the quantum Hall state, Phys. Rev. B **82**, 184516 (2010).

[4] X.-L. Qi, T. L. Hughes, and S.-C. Zhang, Topological field theory of time-reversal invariant insulators, Phys. Rev. B **78**, 195424 (2008).

[5] D. Xiao, J. Jiang, J. H. Shin, W. B. Wang, F. Wang, Y. F. Zhao, C. X. Liu, W. D. Wu, M. H. W. Chan, N. Samarth, and C. Z. Chang, Realization of the Axion insulator state in quantum anomalous Hall sandwich heterostructures, Phys. Rev. Lett. **120**, 056801 (2018).
[6] C. Z. Chang, J. S. Zhang, X. Feng, J. Shen, Z. C. Zhang, M. H. Guo, K. Li, Y. B. Ou, P. Wei, L. L. Wang, Z. Q. Ji, Y. Feng, S. H. Ji, X. Chen, J. F. Jia, X. Dai, Z. Fang, S. C. Zhang, K. He, Y. Y. Wang, L. Lu, X. C. Ma, and Q. K. Xue, Experimental observation of the quantum anomalous Hall effect in a magnetic topological insulator, Science **340**, 167 (2013).
[7] S. Qi, Z. Qiao, X. Deng, E. D. Cubuk, H. Chen, W. Zhu, E. Kaxiras, S. B. Zhang, X. Xu, and Z. Zhang, High-temperature quantum anomalous Hall effect in n-p codoped topological insulators, Phys. Rev. Lett. **117**, 056804 (2016).
[8] Z. Qiao, S. A. Yang, W. Feng, W.-K. Tse, J. Ding, Y. Yao, J. Wang, and Q. Niu, Quantum anomalous Hall effect in graphene from Rashba and exchange effects, Phys. Rev. B **82**, 161414(R) (2010).
[9] H. Zhang, C. Lazo, S. Blügel, S. Heinze, and Y. Mokrousov, Electrically tunable quantum anomalous Hall effect in graphene decorated by 5d transition-metal adatoms, Phys. Rev. Lett. **108**, 056802 (2012).
[10] Z. Qiao, W. Ren, H. Chen, L. Bellaiche, Z. Zhang, A. H. MacDonald, and Q. Niu, Quantum anomalous Hall effect in graphene proximity coupled to an antiferromagnetic insulator, Phys. Rev. Lett. **112**, 116404 (2014).
[11] R. Yu, W. Zhang, H.-J. Zhang, S.-C. Zhang, X. Dai, and Z. Fang, Quantized anomalous Hall effect in magnetic topological insulators, Science **329**, 61 (2010).
[12] J. Y. Zhang, B. Zhao, Y. G. Yao, and Z. Q. Yang, Robust quantum anomalous Hall effect in graphene-based van der Waals heterostructures, Phys. Rev. B **92**, 165418 (2015).
[13] J. Y. Zhang, B. Zhao, T. Zhou, Y. Xue, C. L. Ma, and Z. Q. Yang, Strong magnetization and Chern insulators in compressed graphene/CrI_3 van der Waals heterostructures, Phys. Rev. B **97**, 085401 (2018).
[14] L. Z. Zhang, C. W. Park, and M. Yoon, Quantum phase engineering of two-dimensional post-transition metals by substrates: Toward a room-temperature quantum anomalous Hall insulator, Nano Lett. **20**, 7186 (2020).
[15] Z. Liu, Y. L. Han, Y. F. Ren, Q. Niu, and Z. H. Qiao, Van der Waals heterostructure Pt_2HgSe_3/CrI_3 for topological valleytronicsc, Phys. Rev. B **104**, L121403 (2021).
[16] M. M. Otrokov, I. P. Rusinov, M. Blanco-Rey, M. Hoffmann, A. Y. Vyazovskaya, S. V. Eremeev, A. Ernst, P. M. Echenique, A. Arnau, and E. V. Chulkov, Unique thickness-dependent properties of the van der Waals interlayer antiferromagnet $MnBi_2Te_4$ films, Phys. Rev. Lett. **122**, 107202 (2019).
[17] W. Zhu, C. Song, H. Bai, L. Liao, and F. Pan, High Chern number quantum anomalous Hall effect tunable by stacking order in van der Waals topological insulators, Phys. Rev. B **105**, 155122 (2022).
[18] A. L. Sharpe, E. J. Fox, A. W. Barnard, J. Finney, K. Watanabe, T. Taniguchi, M. A. Kastner, and D. Goldhaber-Gordon, Emergent ferromagnetism near three-quarters filling in twisted bilayer graphene, Science **365**, 605 (2019).
[19] G. Chen, A. L. Sharpe, E. J. Fox, Y.-H. Zhang, S. Wang, L. Jiang, B. Lyu, H. Li, K. Watanabe, T. Taniguchi, Z. Shi, T. Senthil, D. Goldhaber-Gordon, Y. Zhang, and F. Wang, Tunable correlated Chern insulator and ferromagnetism in a moiré superlattice, Nature (London) **579**, 56 (2020).
[20] H. Polshyn, J. Zhu, M. A. Kumar, Y. Zhang, F. Yang, C. L. Tschirhart, M. Serlin, K. Watanabe, T. Taniguchi, A. H. MacDonald, and A. F. Young, Electrical switching of magnetic order in an orbital Chern insulator, Nature (London) **588**, 66 (2020).
[21] M. Serlin, C. L. Tschirhart, H. Polshyn, Y. Zhang, J. Zhu, K. Watanabe, T. Taniguchi, L. Balents, and A. F. Young, Intrinsic quantized anomalous Hall effect in a moiré heterostructure, Science **367**, 900 (2020).
[22] Z. F. Wang, Z. Liu, and F. Liu, Quantum anomalous Hall effect in 2D organic topological insulators, Phys. Rev. Lett. **110**, 196801 (2013).
[23] L. Dong, Y. Kim, D. Er, A. M. Rappe, and V. B. Shenoy, Two-dimensional π-conjugated covalent-organic frameworks as quantum anomalous Hall topological insulators, Phys. Rev. Lett. **116**, 096601 (2016).
[24] Y. Jin, Z. Chen, B. Xia, Y. Zhao, R. Wang, and H. Xu, Large-gap quantum anomalous Hall phase in hexagonal organometallic frameworks, Phys. Rev. B **98**, 245127 (2018).
[25] N. Su, W. Jiang, Z. Wang, and F. Liu, Prediction of large gap flat Chern band in a two-dimensional metal-organic framework, Appl. Phys. Lett. **112**, 033301 (2018).
[26] X. Zhang, Y. Li, T. He, M. Zhao, L. Jin, C. Liu, X. Dai, Y. Liu, H. Yuan, and G. Liu, Time-reversal symmetry breaking Weyl semimetal and tunable quantum anomalous Hall effect in a two-dimensional metal-organic framework, Phys. Rev. B **108**, 054404 (2023).
[27] C. X. Huang, J. Zhou, H. P. Wu, K. M. Deng, P. Jena, and E. J. Kan, Quantum anomalous Hall effect in ferromagnetic transition metal halides, Phys. Rev. B **95**, 045113 (2017).
[28] X. J. Liu, J. Y. Zhang, Y. Wang, H. R. Bao, Y. Qi, and Z. Q. Yang, Prediction of high Curie-temperature intrinsic ferromagnetic semiconductors and quantum anomalous Hall states in XBr_3 (X = Cu, Ag, Au) monolayers, J. Mater. Chem. C **10**, 6497 (2022).
[29] Y. Jiao, X.-T. Zeng, C. Chen, Z. Gao, K. Song, X.-L. Sheng, and S. A. Yang, Monolayer and bilayer $PtCl_3$: Energetics, magnetism, and band topology, Phys. Rev. B **107**, 075436 (2023).
[30] H. P. Wang, W. Luo, and H. J. Xiang, Prediction of high-temperature quantum anomalous Hall effect in two-dimensional transition-metal oxides, Phys. Rev. B **95**, 125430 (2017).
[31] Z. Li, Y. Han, and Z. Qiao, Chern number tunable quantum anomalous Hall effect in monolayer transitional metal oxides via manipulating magnetization orientation, Phys. Rev. Lett. **129**, 036801 (2022).
[32] P.-J. Guo, Z.-X. Liu, and Z.-Y. Lu, Quantum anomalous Hall effect in collinear antiferromagnetism, npj Comput. Mater. **9**, 70 (2023).
[33] B. Wu, Y.-L. Song, W.-X. Ji, P.-J. Wang, S.-F. Zhang, and C.-W. Zhang, Quantum anomalous Hall effect in an antiferromagnetic monolayer of MoO, Phys. Rev. B **107**, 214419 (2023).
[34] N. D. Mermin and H. Wagner, Absence of ferromagnetism or antiferromagnetism in one- or two-dimensional isotropic Heisenberg models, Phys. Rev. Lett. **17**, 1133 (1966).
[35] G. Kresse and D. Joubert, From ultrasoft pseudopotentials to the projector augmented-wave method, Phys. Rev. B **59**, 1758 (1999).

[36] G. Kresse and J. Hafner, Ab initio molecular dynamics for liquid metals, Phys. Rev. B **47**, 558 (1993).

[37] G. Kresse and J. Furthmüller, Efficient iterative schemes for ab initio total-energy calculations using a plane-wave basis set, Phys. Rev. B **54**, 11169 (1996).

[38] P. Hohenberg and W. Kohn, Inhomogeneous electron gas, Phys. Rev. **136**, B864 (1964).

[39] W. Kohn and L. J. Sham, Self-consistent equations including exchange and correlation effects, Phys. Rev. **140**, A1133 (1965).

[40] D. M. Ceperley and B. J. Alder, Ground state of the electron gas by a stochastic method, Phys. Rev. Lett. **45**, 566 (1980).

[41] J. P. Perdew and A. Zunger, Self-interaction correction to density-functional approximations for many-electron systems, Phys. Rev. B **23**, 5048 (1981).

[42] J. P. Perdew, K. Burke, and M. Ernzerhof, Generalized gradient approximation made simple, Phys. Rev. Lett. **77**, 3865 (1996).

[43] B. Anasori, C. Shi, E. J. Moon, Y. Xie, C. A. Voigt, P. R. C. Kent, S. J. May, S. J. L. Billinge, M. W. Barsoum, and Y. Gogotsi, Control of electronic properties of 2D carbides (MXenes) by manipulating their transition metal layers, Nanoscale Horiz. **1**, 227 (2016).

[44] X. Zhang, J. Wei, R. Li, C. Zhang, H. Zhang, P. Han, and C. Fan, DFT + U predictions: Structural stability, electronic and optical properties, oxidation activity of BiOCl photocatalysts with 3d transition metals doping, J. Mater. Sci. **53**, 4494 (2018).

[45] X. Yao, J. Ji, Y. Lin, Y. Sun, L. Wang, A. He, B. Wang, P. Lu, M. He, and X. Zhang, TMB_2C (TM = Ti, V): 2D transition metal borocarbide monolayer with intriguing electronic, magnetic and electrochemical properties, Appl. Surf. Sci. **605**, 154692 (2022).

[46] A. Togo and I. Tanaka, First principles phonon calculations in materials science, Scr. Mater. **108**, 1 (2015).

[47] U. Wolff, Collective Monte Carlo updating for spin systems, Phys. Rev. Lett. **62**, 361 (1989).

[48] A. A. Mostofi, J. R. Yates, Y.-S. Lee, I. Souza, D. Vanderbilt, and N. Marzari, Wannier90: A tool for obtaining maximally-localised Wannier functions, Comput. Phys. Commun. **178**, 685 (2008).

[49] N. Marzari and D. Vanderbilt, Maximally localized generalized Wannier functions for composite energy bands, Phys. Rev. B **56**, 12847 (1997).

[50] Q. Wu, S. Zhang, H.-F. Song, M. Troyer, and A. A. Soluyanov, WannierTools: An open-source software package for novel topological materials, Comput. Phys. Commun. **224**, 405 (2018).

[51] N. Mounet, M. Gibertini, P. Schwaller, D. Campi, A. Merkys, A. Marrazzo, T. Sohier, I. E. Castelli, A. Cepellotti, G. Pizzi, and N. Marzari, Two-dimensional materials from high-throughput computational exfoliation of experimentally known compounds, Nat. Nanotechnol. **13**, 246 (2018).

[52] See Supplemental Material at http://link.aps.org/supplemental/10.1103/PhysRevB.108.214427 for detailed information about the magnetic configurations of Ti_3O_5 monolayer; the schematic diagram and band structure of artificial My mirror breaking of Ti_3O_5 monolayer; the band structures of Ti_3O_5 monolayer with in-plane magnetization; the band strucure, edge state and anomalous Hall conductivity of Ti_3O_5 monolayer when magnetization is along -z direction; and the band structure and MAE of Ti_3O_5 monolayer under strains.

[53] J. B. Goodenough, Theory of the role of covalence in the perovskite-type manganites [La,M(II)] MnO_3, Phys. Rev. **100**, 564 (1955).

[54] P. W. Anderson, New approach to the theory of superexchange interactions, Phys. Rev. **115**, 2 (1959).

[55] J. Kanamori, Crystal distortion in magnetic compounds, J. Appl. Phys. **31**, S14 (1960).

[56] Z. Liu, G. Zhao, B. Liu, Z. F. Wang, J. Yang, and F. Liu, Intrinsic quantum anomalous Hall effect with in-plane magnetization: Searching rule and material prediction, Phys. Rev. Lett. **121**, 246401 (2018).

[57] C. Niu, J.-P. Hanke, P. M. Buhl, H. Zhang, L. Plucinski, D. Wortmann, S. Blügel, G. Bihlmayer, and Y. Mokrousov, Mixed topological semimetals driven by orbital complexity in two-dimensional ferromagnets, Nat. Commun. **10**, 3179 (2019).

[58] X. Wu, R. Li, X. Zou, B. Huang, Y. Dai, and C. Niu, Robust quantum anomalous Hall effect with tunable magnetization directions and Chern numbers, Phys. Rev. B **108**, 115438 (2023).